Eur. Phys. J. E (2013) **36**: 85
DOI 10.1140/epje/i2013-13085-0

THE EUROPEAN PHYSICAL JOURNAL E

Regular Article

Low Reynolds number suspension gravity currents

Sandeep Saha[1,2], Dominique Salin[1,2,a], and Laurent Talon[1,2]

[1] UPMC Univ Paris 06, Univ Paris-Sud, CNRS, F-91405, France
[2] Lab FAST, Bat 502, Campus Univ, Orsay, F-91405, France

Received 29 January 2013 and Received in final form 3 June 2013
Published online: 13 August 2013 –

Abstract. The extension of a gravity current in a lock-exchange problem, proceeds as square root of time in the viscous-buoyancy phase, where there is a balance between gravitational and viscous forces. In the presence of particles however, this scenario is drastically altered, because sedimentation reduces the motive gravitational force and introduces a finite distance and time at which the gravity current halts. We investigate the spreading of low Reynolds number suspension gravity currents using a novel approach based on the Lattice-Boltzmann (LB) method. The suspension is modeled as a continuous medium with a concentration-dependent viscosity. The settling of particles is simulated using a drift flux function approach that enables us to capture sudden discontinuities in particle concentration that travel as kinematic shock waves. Thereafter a numerical investigation of lock-exchange flows between pure fluids of unequal viscosity, reveals the existence of wall layers which reduce the spreading rate substantially compared to the lubrication theory prediction. In suspension gravity currents, we observe that the settling of particles leads to the formation of two additional fronts: a horizontal front near the top that descends vertically and a sediment layer at the bottom which aggrandises due to deposition of particles. Three phases are identified in the spreading process: the final corresponding to the mutual approach of the two horizontal fronts while the laterally advancing front halts indicating that the suspension current stops even before all the particles have settled. The first two regimes represent a constant and a decreasing spreading rate respectively. Finally we conduct experiments to substantiate the conclusions of our numerical and theoretical investigation.

1 Introduction

The horizontal intrusion of a fluid into another, driven by a density difference is known as a *gravity current* [1,2]. Following the pioneering works of [3,4] gravity currents have been studied extensively for many decades now, primarily due to their relevance to numerous industrial and environmental setups. Engineering problems like the infiltration of saline water into fresh water upon the release of a lock gate [5], mixing of miscible fluids in chemical and petroleum refineries [6–10] and environmental hazards like spreading of lava domes [11], oil spills [12] and avalanches [1], all involve gravity currents. Among the scenarios mentioned, suspension gravity currents comprise a unique variety since the origin of buoyancy is not a denser fluid but the suspended particles. Hence, the dynamics of the gravity current is intricately linked to the settling and entrainment processes of the particles [13,14]. The implications can be far reaching, for instance: turbidity currents which originate along a continental slope proceed swiftly through submarine canyons and run out upon arriving at the ocean basin and on occasions form large reserves of oil [15,16]. Estimates of the run out distance of similar particle-laden flows like avalanches and mudslides is equally important for assessing and mitigating the associated risks. Thus a better understanding of suspension gravity currents is warranted for improving environmental hazard predictions.

The investigation of the extent of spreading of an oil spill in a calm sea, revealed the presence of three regimes in the spreading process [12]: during the initial stages, the gravitational force is balanced by inertia (inertia-buoyancy phase), whilst later when the current has spread over a distance much larger than its thickness the viscous forces balance out gravity (viscous-buoyancy phase). The final regime concerns long time spreading where the gravitational force itself is negligible and the currents spreads under the action of surface tension and viscous forces. However, for particle-laden flows only the inertial and viscous-buoyancy phases are relevant due to the absence of surface tension. A significant portion of the literature on non-Brownian suspension gravity currents is dedicated to inertial-buoyancy phase owing to the widespread applications like pyroclastic flows, turbidity currents, pollutant dispersion from industrial effluents, transport of sediment by rivers where the characteristic velocities are high [14, 17–21].

In this article we focus on suspension gravity currents which belong to the viscous buoyancy phase. Such currents

[a] e-mail: salin@fast.u-psud.fr

are pertinent to mud slurries flowing in subterranean fractures, where the characteristic length-scales can be very small (on the order of a millimeter) for inertial effects to be of any significance. In such particle-laden currents the buoyancy force reduces over time as the particles settle out and as a result the current is arrested at a downstream location. Similar observations were reported in the experiments on the spreading dynamics of suspension currents in the inertial buoyancy phase [17]. The authors found that the high-concentration suspension currents come to an "abrupt halt" at a location which they refer to as the run out length. The run out length was reported to increase for concentrations lower than a critical value and decrease subsequently for the higher concentrations. A comparison to the "box model" approach [14], yielded good agreement with experimental data at low concentrations but was inconclusive for high concentrations. Since the "box model" is valid only for very dilute suspensions, the authors emphasised the need for an alternative theoretical approach. Furthermore, other pertinent questions about the dependence of the run out length on particle size and the properties of the interstitial fluid have not yet received a satisfactory explanation. Therefore, our primary aim is to gain an understanding of the physical processes governing the run out length and its dependence on various parameters like concentration and particle size.

In order to conduct the current investigation, we develop a novel modeling approach based on the Lattice-Boltzmann (LB) method for suspension flows which qualitatively replicates experimental observations and yields data for comparison with theoretical models. The LB method is used to solve simple model equations which retain the essential physical processes at play for example, sedimentation, rheology and buoyancy, present in the problem. The simplifications underlying the proposed model are necessary because the exact constitutive laws governing the flow of suspensions are under debate in the scientific community. For instance, critical issues related to the precise rheology of suspensions which includes knowledge of the volume fraction at which viscosity diverges, shear-thinning power law, magnitude of yield stress and the influence of particle size and distribution are yet to be addressed satisfactorily [22,23]. In order to avoid these contentious issues, we incorporated a concentration-dependent Newtonian rheology for the suspension in our model. We adopt a three pronged approach, wherein we perform a parametric study using two-dimensional LB simulations, which provides the necessary insight to develop a lubrication theory based one-dimensional model. Finally, we perform experiments to confirm the observations from the numerical investigation, but make no attempt to match quantitatively the experimental data because of the difference in the geometries of the two: The experiments are performed in a three-dimensional rectangular Hele-Shaw cell whereas the LB simulations are conducted for a two-dimensional tank.

A multitude of methods have been applied to model suspensions like Stokesian dynamics [24], dissipative particle dynamics [25], Lattice-Boltzmann method [26], Lagrange multiplier fictitious domain method [27] and they require varying levels of computational effort. We model the suspension as a fluid at the macroscopic level which obeys the laws of continuum mechanics and incorporate the hydrodynamic forces acting on the particles using simple constitutive laws for the settling velocity [28–30] and the rheological properties [22,31]. This approach allows us to achieve a computationally efficient model and hence is ideally suited for large parametric studies and construction of analytical models.

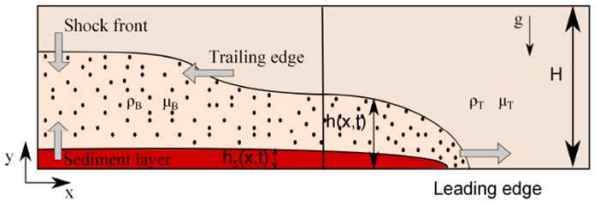

Fig. 1. A schematic of the lock-exchange between a suspension and a clear fluid.

In this paper, we apply our novel approach to study a lock-exchange flow setup by releasing a dense suspension (with density and viscosity ρ_B, μ_B respectively) into the suspending clear fluid (with density and viscosity ρ_T, μ_T respectively) in a tank of height H as shown in fig. 1. A suspension current is setup instantaneously, which is driven by the density difference, $\Delta\rho \equiv \rho_B - \rho_T$. Simultaneously, the settling of particles creates a vertically descending horizontal front, $h(x,t)$, near the top and a vertically ascending sediment front, $h_s(x,t)$, at the bottom. The evolution of these fronts is examined in the forthcoming sections.

This article is structured as follows: sect. 2 describes the numerical model and a brief summary of the solution technique. In order to demonstrate the validity of the model we present validation cases for sedimentation in vertical and inclined tanks. Section 3 presents the results for a lock-exchange flow between the suspension and the clear suspending fluid in the absence of sedimentation. We thus delineate the effects of increasing viscosity and gravitational body force which arise from increasing particle concentration. Thereafter, we study the same problem in the presence of sedimentation in sect. 4 and present the effects of variation in particle size and concentration. Finally, concluding remarks are made in sect. 5 followed by appendix A where the derivation of the flux function based on lubrication theory is presented.

2 Numerical simulations

2.1 The governing equations and boundary conditions

We first consider a suspension consisting of an interstitial fluid and particles as a continuous medium which can be represented by volume averaged velocities $\boldsymbol{u} \equiv (1-\varphi)\boldsymbol{u}_f + \varphi\boldsymbol{u}_p$ and kinematic viscosity $\nu(\varphi)$. Such an approach is valid when we consider length-scales greater than $\gtrsim 100$ particle diameters [32]. We assume that the suspension is a Newtonian fluid whose viscosity depends on the local particle concentration, φ. Such an assumption is reasonable for particle concentrations not close to

the packing fraction [22]. Furthermore, we assume that Boussinesq approximation is applicable to the flow which implies that the relative density difference between the suspended particles and the fluid is small. The application of this approximation to the governing equations leads to significant simplification. For non-Boussinesq flows, additional terms arising from the relative density difference must be retained in the momentum equations. Under these conditions, the continuity and momentum equations can be expressed as

$$\bigtriangledown \cdot \boldsymbol{u} = 0, \tag{1}$$

$$\frac{\partial \boldsymbol{u}}{\partial t} + \boldsymbol{u} \cdot \bigtriangledown \boldsymbol{u} = -\frac{1}{\rho} \bigtriangledown P + \frac{\rho_p - \rho_f}{\rho} \varphi \boldsymbol{g} + \bigtriangledown \cdot \big(\nu(\varphi) \bigtriangledown \boldsymbol{u}\big), \tag{2}$$

where $\rho \equiv (1-\varphi)\rho_f + \varphi\rho_p$ represents the density and the subscripts p, f denote the particle and the fluid phases, respectively. Since we apply the Boussinesq approximation, $\rho_p \simeq \rho_f \simeq \rho$ but $(\rho_p - \rho_f)g$ may not be negligible and represents the buoyancy force. In general, the rheology of suspensions depends on other factors as well for example the particle dispersivity and shape. In this study we restrict ourselves to suspensions comprising of monodisperse, spherical particles with a rheology characterised by [31]

$$\nu(\varphi) = \nu_f \left(1 - \frac{\varphi}{\varphi_j}\right)^{-2}, \tag{3}$$

where, $\varphi_j \sim 0.61$ is the jamming concentration [22]. We note that accurate modeling of the rheology of a suspension, close to the packing fraction, is still under scientific debate [23,33,34]. However, in the vicinity of packing fraction, the nearly compacted sediment flows very slowly in any model, either due to the divergence of local viscosity or because of yielding.

The sedimentation Reynolds number defined as $Re_s \equiv u_0 H/\nu$ [35] in our simulations is in the range $[0.025, 0.25]$. Since our interest lies in the viscous-buoyancy phase where the inertial force is much weaker than the viscous and gravitational body forces, we examined whether the exclusion of inertial terms affects our results. We observe that indeed the inertial terms when excluded from our computations, do not affect the spreading of the gravity current.

The particle concentration is governed by a convection-diffusion equation,

$$\frac{\partial \varphi}{\partial t} + \bigtriangledown \cdot (\varphi \boldsymbol{u} + \varphi \mathscr{V}(\varphi)) = D_0 \Delta \varphi, \tag{4}$$

where, D_0 is the hydrodynamic self-diffusion [36–38] and $\mathscr{V}(\varphi)$ is the hindered settling velocity function which represents the slip velocity of particles in a suspension. Our analysis uses the well established hindrance velocity model [39,28,40]

$$\begin{aligned} \mathscr{V}(\varphi) &= (1-\varphi)^5 \boldsymbol{u}_0; \qquad && \varphi < \varphi_s, \\ \mathscr{V}(\varphi) &= \boldsymbol{0}; && \varphi \geq \varphi_s, \end{aligned} \tag{5}$$

where

$$\boldsymbol{u}_0 \equiv \frac{2a^2(\rho_p - \rho_f)\boldsymbol{g}}{9\rho_f \nu_f} \tag{6}$$

is the Stokes settling velocity of a particle with radius a and $\varphi_s = 0.57$ is the maximum concentration of the suspension beyond which the particles are immobile with respect to the fluid [39]. The flux function which is defined as the product $\varphi\mathscr{V}(\varphi)$ has been determined experimentally [39] and was reported to be discontinuous at $\varphi_s = 0.57$, a value corresponding to random loose packing. It must be noted that φ_s is distinct from φ_j and the precise values are still a subject of active research [22]. It should also be pointed out that D_0 is a function of φ but the dependence has not been well established [36–38]. We have therefore assumed D_0 to be constant and its value is typically in the range $D_0 \sim 8au_0 \sim 10^{-4}$ [36].

The no-slip and no-penetration boundary conditions are implemented at the wall and a no normal-flux condition is implemented at the boundaries for the concentration field. It is customary for simulations performed using a LB code, that lengths are prescribed in terms of lattice units (δx) and time in terms of unit time step (δt). Therefore, in the following velocities are expressed in terms of $\delta x/\delta t$ and g in terms of $\delta x/(\delta t)^2$.

2.2 The Lattice-Boltzmann scheme

In order to solve the momentum equation (2) and the transport equation (4), we implement a Two-Relaxation-Times (TRT) Lattice-Boltzmann scheme.

2.2.1 The TRT scheme for momentum equation

Modeling of the Stokes and Navier-Stokes equations with the TRT operator is discussed in detail in [41]. In the present work, we use the D2Q9 Navier-Stokes scheme where the unknown variables are the 9 population vectors $\{f_q,\ q = 0, \ldots, 8\}$. The Lattice-Boltzmann scheme can be split into two steps. The collision step which redistributes the populations $f_q \rightarrow \tilde{f}_q$ and the propagation step $f_q(\boldsymbol{r} + \boldsymbol{c}_q, t+1) = \tilde{f}_q$ which translates the populations according to their velocity, $\boldsymbol{c}_q$, from a position, $\boldsymbol{r}$.

The collision step definition allows us to characterise the fluid properties. We introduce the notation $\boldsymbol{c}_{\bar{q}} = -\boldsymbol{c}_q$ for the direction opposite to the velocity vector $\boldsymbol{c}_q$ and we order the populations such that for all $q \in [1;4]$ are opposite to the corresponding $q \in [5;8]$. The TRT collision operates on the symmetric ($f_q^+ = (f_q + f_{\bar{q}})/2$) and the anti-symmetric ($f_q^- = (f_q - f_{\bar{q}})/2$) components for $q = 1, \ldots, 4$. It is performed by prescribing the two equilibrium distributions $\{e_q^{\pm}\}$ and two collision eigenvalues $\lambda^{\pm} \in]0, 2[$. The eigenvalue, λ^+, pertains to all symmetric non-equilibrium components, $\{n_q^+\}$ and similarly λ^- for all anti-symmetric non-equilibrium components $\{n_q^-\}$. Hence the collision step can be expressed as

$$\tilde{f}_0 = \left[f_0(1-\lambda^+) + \lambda^+ e_0\right](\boldsymbol{r}, t), \tag{7}$$

$$\tilde{f}_q = \left[f_q - \lambda^+ n_q^+ - \lambda^- n_q^- + S_q^-\right](\boldsymbol{r}, t), \quad q = 1 \ldots 4, \tag{8}$$

$$\tilde{f}_{\bar{q}} = \left[f_{\bar{q}} - \lambda^+ n_q^+ + \lambda^- n_q^- - S_q^-\right](\boldsymbol{r}, t), \quad q = 1 \ldots 4, \tag{9}$$

where S_q^- is an external momentum source which allows imposition of a body force $\boldsymbol{F}$ and $n_q^\pm = (f_q^\pm - e_q^\pm), q = 1 \ldots 4$.

Fluid dynamical entities are obtained by the prescription of the equilibrium functions $e_q^\pm$, which in turn requires the computation of the local macroscopic quantities: the mass

$$\rho = \sum_{q=0}^{9} f_q = f_0 + 2\sum_{q=1}^{4} f_q^+, \tag{10}$$

and momentum

$$\boldsymbol{J} = \sum_{q=1}^{9} f_q \boldsymbol{c}_q = 2\sum_{q=1}^{4} f_q^- \boldsymbol{c}_q. \tag{11}$$

The equilibrium functions are defined as

$$e_q^+ = t_q^\star \left(c_s^2 \rho + \frac{3(\boldsymbol{J}\cdot\boldsymbol{c}_q)^2 - \boldsymbol{J}\cdot\boldsymbol{J}}{2\rho_0} \right),$$

$$e_q^- = t_q^\star (\boldsymbol{J}\cdot\boldsymbol{c}_q), \qquad e_0 = \rho - 2\sum_{q=1}^{4} e_q^+,$$

$$S_q^- = t_q^\star \boldsymbol{F}\cdot\boldsymbol{c}_q,$$

where the weights $\{t_q^\star\}$ are isotropic and take the value $t_q^\star = \{\frac{1}{3}, \frac{1}{12}\}$ for the first and second (diagonal) neighbour links respectively in the D2Q9 model. The quantity, ρ_0 is a constant and represents the average mass of the domain.

The local pressure $P = c_s^2\rho$ and the local velocity $\boldsymbol{u} = \frac{1}{\rho_0}\sum_{q=1}^{9} f_q \boldsymbol{c}_q + \frac{1}{2}\boldsymbol{F}$ thus satisfy the momentum equation (2) The viscosity is given by the even eigenvalue $\nu = \frac{1}{3}(\frac{1}{\lambda^+} - \frac{1}{2})$. For improving the numerical precision [41], the second eigenvalue λ^- is chosen so as to keep the coefficient $\Lambda = (\frac{1}{\lambda^-} - \frac{1}{2})(\frac{1}{\lambda^+} - \frac{1}{2})$ constant. In the present work, we use $\Lambda = 0.25$.

2.2.2 The particle-transport equation

To implement the transport equation, we use a scheme similar to [42]. We define another set of 9-population vectors $\{f_q,\ q = 0, \ldots, 8\}$, and thereafter the propagation-collision step is computed according to: $f_q(\boldsymbol{r} + \boldsymbol{c}_q, t+1) = \tilde{f}_q$ and eqs. (7)–(9) with $S_q^- = 0$.

The equilibrium distributions require the computation of the local volume fraction, $\varphi = \sum_{q=0}^{9} f_q = f_0 + 2\sum_{q=1}^{4} f_q^+$ and are given by

$$e_q^+ = \varphi \left(t_q^* c_e + \frac{1}{4}(u_x^2 - u_y^2) p_q^{xx} + \frac{1}{4}(u_x u_y) p_q^{xy} + t_q^* \frac{1}{2} U^2 \right),$$

$$e_q^- = \varphi(\boldsymbol{u} + \boldsymbol{V}(\varphi))\cdot\boldsymbol{c}_q,$$

$$e_0^+ = \varphi\left(1 - \sum_{q=1}^{9} e_q^+\right),$$

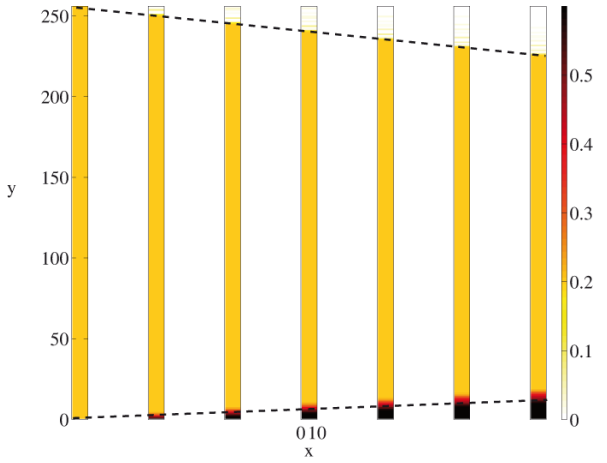

Fig. 2. Sedimentation of a suspension with $\varphi_0 = 0.2$, $H = 256$ δx and $u_0 = 10^{-3}\delta x/\delta t$, showing the evolution of two fronts: one between suspension and clear fluid near the top wall and another between the sediment layer and the suspension close to the bottom wall. The leftmost snapshot is a $t = 0$ and each subsequent snapshot is $1.5 \times 10^4 \delta t$ later.

where $t_q^* = \{\frac{1}{4}, \frac{1}{8}\}$ for the first and second (diagonal) neighbour links respectively and $p_q^{xx} = c_{qx}^2 - c_{qy}^2$ and $p_q^{xy} = c_{qx}c_{qy}$. Thus the concentration, φ satisfies a convection-diffusion equation (4) where the diffusion coefficient is given by $D_0 = c_e(\frac{1}{\lambda^-} - \frac{1}{2})$. The other relaxation parameter, λ^-, is chosen such that the parameters $\Lambda = (\frac{1}{\lambda^-} - \frac{1}{2})(\frac{1}{\lambda^+} - \frac{1}{2}) = 0.25$ and $c_e^2 = 1/3$ are held fixed.

2.3 Validation

2.3.1 Vertical tank

The settling of particles in a suspension with homogeneous initial concentration, $\varphi(x, y) = \varphi_0$ in a vertical tank was simulated using the numerical procedure presented in subsect. 2.2. The settling of the particles can lead to the formation of multiple shock fronts, that is localised regions of discontinuous or sharp gradients in particle concentration, due to the hindered settling velocity eqs. (5) [29]. One such front exists between the suspension and the clear fluid at the top as illustrated by fig. 2. The front descends towards the bottom at a constant velocity $u_T(\varphi)$. Another front develops due to the deposition of particles at the bottom of the tank that gradually ascends upwards also at a constant velocity $u_B(\varphi)$. Figure 2 shows the accretion of this sediment layer at various instants of time. The front however is not as sharp as the top front due to hydrodynamic diffusion.

The velocity of a shock front at a height, h, can be determined from the particle transport equation (4) [29]

$$\mathcal{V}(\varphi) = \frac{\varphi(h^+)\mathscr{V}(\varphi(h^+)) - \varphi(h^-)\mathscr{V}(\varphi(h^-))}{\varphi(h^+) - \varphi(h^-)}, \tag{12}$$

where $h^\pm$ denote y locations just above and below the shock respectively. In the presence of small but finite

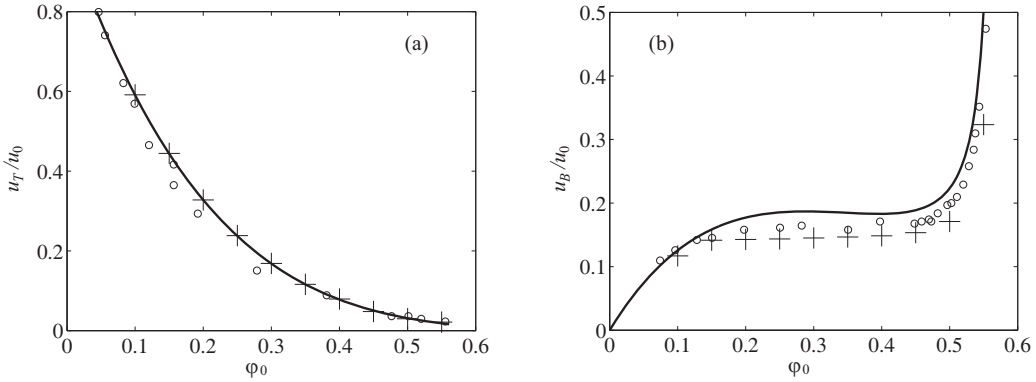

Fig. 3. Comparison of experimental data, theoretically predicted and numerically obtained shock front velocity of (a) suspension layer, $u_T(\varphi)$, and (b) sediment layer, $u_B(\varphi)$, for various initial concentrations φ_0. —— theoretical curve from eq. (12), + numerical simulation with $H = 256$ and $u_0 = 10^{-3}$, ∘ experimental data [39].

hydrodynamic diffusion, although the shock front is regularised, the front velocity remains unaltered [43]. The location of the shock front between the suspension and clear fluid was traced by computing the contour associated with φ_0 which is largely horizontal except near the walls. The velocity of the top shock front, $u_T(\varphi)$, is computed and compared to the theoretical curve $\mathcal{V}(\varphi_0)$ (12) for various φ_0 in fig. 3(a). There is a very good agreement between the two curves.

The rate of ascent of the sediment layer, $u_B(\varphi_0)$, was computed from the concentration contour level, $\varphi = \varphi_s$, and compared to eq. (12) which predicts the front velocity as $\mathcal{V}(\varphi_0)\frac{\varphi_0}{\varphi_s - \varphi_0}$. There is a reasonable match for low concentrations ($\varphi_0 < 0.2$) between the data from the Lattice-Boltzmann simulations and eq. (12). At higher concentrations there is a small discrepancy which is due to the thickening of the front as opposed to a self-sharpening shock front [29]. Therefore eq. (12) is not strictly applicable and only provides an approximation of the ascent of the sediment layer in this case. In contrast, our simulation results match well with the experimental data [39] for the entire range investigated.

2.3.2 Inclined tank

The velocity of a shock wave is constant over time in a vertical tank but a slight inclination of the tank results in a significant enhancement of the settling velocity due to the well-known Boycott effect [44]. The sedimentation of the particles was simulated in an inclined tank in order to test the ability of the numerical code to replicate the enhancement in settling velocity.

The tilting of the tank leads to an increase in the area over which the particles can settle when compared to the vertical tank. However, the area available for the downward displacement of the interface remains fixed. Hence the additional clear fluid generated due to the settling of particles necessitates an enhancement in the shock front velocity in order to ensure conservation of mass [35]. Figure 4 shows the evolution of the concentration field with time for a suspension in an inclined tank. A shock front

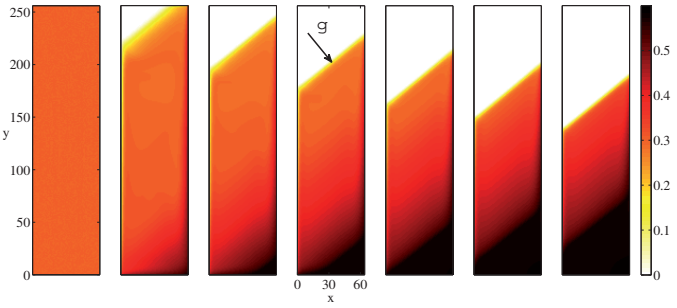

Fig. 4. The evolution of two fronts: one between the clear fluid and the suspension and the accretion of the sediment layer in an inclined tank. The leftmost snapshot is a $t = 0$ and each subsequent snapshot is $2.29 \times 10^5 \delta t$ later. $\varphi_0 = 0.3$, $u_0 = 2 \times 10^{-3}$, $H = 256$ and $\alpha = 40°$.

demarcates the clear fluid from the suspension. A part of the front is perpendicular to the gravity whereas the rest of the front separates a tiny layer of clear fluid adjacent to the downward facing wall from the suspension. The Ponder-Nakamura-Koruda (PNK) model [45,46] hypothesizes that the thickness of this layer, denoted by δ, remains nearly constant with time. As a consequence the clear fluid generated underneath the shock front must appear above the downward moving interface thus enhancing the settling velocity. A similar physical process can be observed in our simulations as well. Figure 5(a) compares the thickness of the clear fluid layer at different instants of time and it remains nearly constant and matches well with the analytical prediction of [35].

Based on the physical argument of PNK theory the shock front velocity is enhanced according to,

$$\frac{\mathrm{d}h}{\mathrm{d}t} = -\mathcal{V}(\varphi)\left(1 + \frac{h}{b}\sin\alpha\right), \tag{13}$$

where h is the location of the front, b is the tank width, α is the angle of inclination and $\mathcal{V}(\varphi)$ is the shock front velocity in a vertical tank. However if the height of the suspension is comparable to the sediment layer at the bottom, the increasing thickness of the sediment layer must

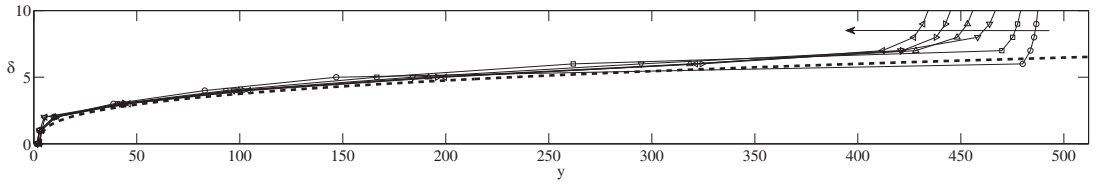

Fig. 5. (a) Comparison of theoretically predicted [35] (– – –) and numerically obtained thickness of the clear fluid layer at different instants of time. Starting from $t = 2 \times 10^5$ onwards to $t = 4.5 \times 10^5$ every $5 \times 10^4 \delta t$ and the arrow points in the direction of increasing time. $\varphi_0 = 0.1$, $u_0 = 10^{-4}$, $H = 512$ and $\alpha = 20°$.

be accounted for, in the settling velocity calculations [35]. The presence of the sediment layer inhibits the settling velocity since the effective height is only $h - h_s$, where h_s is the height of the sediment layer. Therefore eq. (13) is rewritten as

$$v = -v_0\left(1 + \frac{h - h_s}{b}\sin\alpha\right). \tag{14}$$

In addition, conservation of mass of the particles requires,

$$\frac{\mathrm{d}}{\mathrm{d}t}\big((h - h_s)\varphi_0 + h_s\varphi_b\big) = 0, \tag{15}$$

where φ_b is the concentration of the sedimentation layer. Equations (14) and (15) can be reduced to an ordinary differential equation for $h - h_s$, to which the solution is

$$h - h_s = \left(\frac{b}{\sin\alpha} + h(0) - h_s(0)\right)e^{-\frac{\varphi_b}{\varphi_0}\frac{v_0 t}{b}\sin\alpha} - \frac{b}{\sin\alpha}. \tag{16}$$

We make a quantitative comparison by tracking the contours of the shock fronts at the top, $\varphi = 0.5\varphi_0$, and at the bottom, $\varphi_b = 0.45$. The difference of these heights, $h - h_s$ is plotted against time in fig. 6 for three different angles of inclination. The data obtained from the simulations agree with the analytic solution (16). In previous experiments [35], φ_b increased with time due to the compaction of the sediment layer. Furthermore, the authors found that φ_b typically lies in the range $[0.43, 0.53]$. In our computations we find that a unique value $\varphi_b = 0.45$ gives good agreement with the simulation data and lies in the experimental range of [35].

3 The lock-exchange problem with only viscosity contrast

The previous section demonstrated the effect of particle concentration on the settling velocity of sedimentation fronts and the aggrandisement of the sediment layer. In addition, the variation in concentration also affects the flow characteristics of the suspension by altering its viscosity and the gravitational body force acting per unit volume. Therefore, the overall effect of increase in φ on the extension of particle-laden gravity current is not evident. To gain a better understanding we distinguish, in this section, the effects of concentration variation on the flow characteristics *only* by examining the lock-exchange

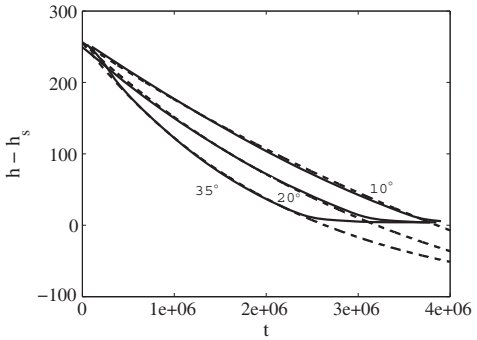

Fig. 6. The difference between the heights of two shock fronts, $h - h_s$ as a function of time for different angles of inclination. —— numerical simulation; – – – analytical solution (16). $\varphi_0 = 0.3$, $u_0 = 2 \times 10^{-4}$, $H = 256$.

between two pure fluids of distinct density and viscosity. In order to simulate the lock-exchange flow, we set, $u_0 = 0$, which is equivalent to setting the particle size equal to 0 and hence the suspension represents the heavier and more viscous fluid. Therefore, in this section, we determine the combined effect of varying the reduced gravity, $\frac{\Delta\rho g}{\rho_T} = \frac{\varphi(\rho_p - \rho_f)g}{\rho_f}$, and the viscosity ratio, $\mu_{BT} \equiv \frac{\mu_B}{\mu_T} = (1 - \frac{\varphi}{\varphi_j})^{-2}$, by changing the concentration, φ, of the suspension.

3.1 LB Simulations

A comparison of the evolution of the gravity current is made for two different viscosity ratios, $\mu_{BT} = 1$ and $\mu_{BT} = 100$. Figure 7(a) shows that the interface is symmetric about the origin when the two fluids have equal viscosities. This observation is in agreement with previous studies [47,48]. However, at a higher viscosity ratio $\mu_{BT} = 100$, the evolution of the interface is markedly different as shown in fig. 7(b). The qualitative differences in the evolution of the two gravity currents can be summarised as follows:

1) The gravity current spreads much slower for $\mu_{BT} = 100$ than $\mu_{BT} = 1$. It is worth noting that the current slows down despite an increase in the gravitational body force, which in principle increases the lateral spreading rate. Since the viscosity ratio is the only other factor which is affected by changing the concentration, the slowing down must be due to an increase in μ_{BT}.

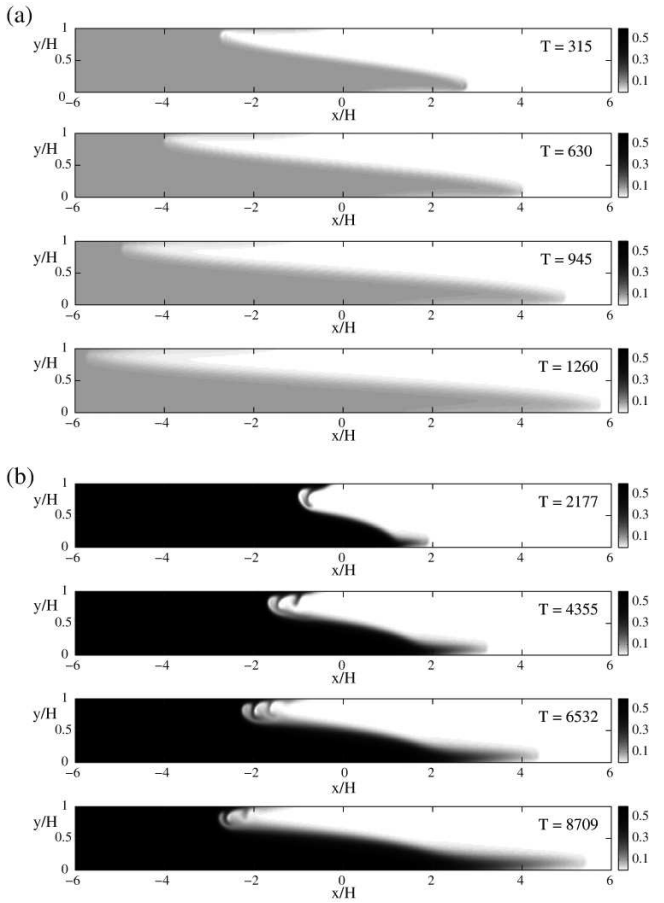

Fig. 7. Evolution of the concentration field with time ((a) $T =$ 316, 630, 945, 1260; (b) $T =$2177, 4355, 6532, 8709), in coordinates normalized by H. (a) $\mu_{BT} = 1$, $D_g = 1.74$, (b) $\mu_{BT} =$ 100, $D_g = 10.06$, where the parameter D_g is defined after eq. (5).

2) The edges of the gravity current are sharp nosed in fig. 7(a). Contrarily, in the case of $\mu_{BT} = 100$ we observe that the trailing edge is blunt while the the leading edge is pointed. The leading edge is also more diffused than the trailing edge.
3) There exists, although thin, a layer of the heavier fluid adjacent to the top wall which leads to gravitational, Rayleigh-Taylor (RT) instabilities behind the trailing edge in fig. 7(b). Such a wall layer is not prominent in fig. 7(a) where viscosities of the two fluids are equal.

Although the interface is markedly different in the two cases, the leading and trailing edges are nearly equidistant from the center for both viscosity ratios. This curious result motivated us to conduct a comparative study with an existing theoretical model based on the classical lubrication approximation [49,47,48]. By assuming a single-valued function, $h(x,t) = y_i/H$ with a small streamwise (x) gradient, to represent the pseudo-interface, where y_i is the wall normal distance of the interface from the bottom wall, an evolution equation for conserving mass can be obtained,

$$\frac{\partial h}{\partial t} + \frac{\partial q}{\partial x} = 0, \tag{17}$$

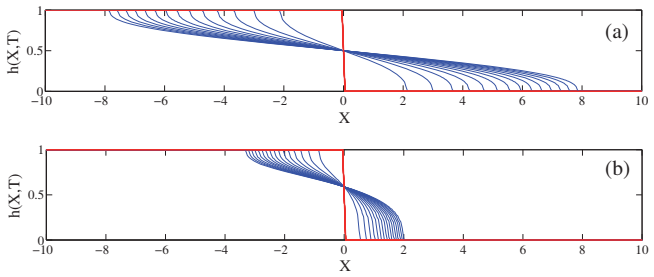

Fig. 8. Evolution of the interface with time obtained from the lubrication model for (a) $\mu_{BT} = 1$ and (b) $\mu_{BT} = 100$. The thick curve corresponds to the initial condition and the rest correspond to different instants of time, 166 time units apart.

where the flux $q(h, \mu_{BT})$ [47],

$$q \equiv \frac{D_g h^3(1-h)^3(h(-1+\mu_{BT})-\mu_{BT})\frac{\partial h}{\partial x}}{(h^4 - 2(-1+h)h(2+(-1+h)h)\mu_{BT} + (-1+h)^4\mu_{BT}^2)}, \tag{18}$$

and $D_g \equiv \frac{\Delta\rho g H^3}{3\mu_T}$. Hence D_g has the units $(\delta x)^2/\delta t$. We chose to non-dimensionalise eq. (17) by the viscosity of the lighter fluid, μ_T, for the latter part of the article which addresses suspensions, where the exact rheology is model dependent.

We solve eq. (17) numerically using an explicit marching scheme. The spatial discretisation was performed using fourth-order central difference scheme and the time marching was performed using the 4th order Runge-Kutta method. The initial condition chosen was a hyperbolic tangent function profile, $h(X,0) = -\frac{\tanh(X/\delta x_0)-1}{2}$ with $\delta x_0 = 10^{-4}$. The code was validated by comparing with the results reported by [47].

The numerical solutions of eq. (17) are plotted in fig. 8(a) and (b) for viscosity ratios $\mu_{BT} = 1$ and 100, respectively. We plot the results in the non-dimensional coordinates $X \equiv x/H$ and $T \equiv \frac{D_g t}{H^2}$. The interface is symmetric when the two fluids are of equal viscosities as can been seen in fig. 8(a), an observation concordant with the numerical simulations. However, fig. 8(b), reveals that although the interface is asymmetric for $\mu_{BT} = 100$, the trailing edge travels significantly faster than the leading edge. In addition, the nose at the trailing edge appears sharper than that of the leading edge. These qualitative observations are in contradiction with the numerical simulations and therefore a quantitative comparison is required to estimate the extent of discrepancy between the 2D simulations and the 1D lubrication model. Quantitatively, the leading and trailing edges are defined as follows: We first binarize the concentration map by evaluating the condition $\psi \geq 0.5\psi_0$. Then, we determine the position at which the vertically averaged concentration map equals 5% and 95% of the total height for the leading and trailing edges respectively.

Figure 9(a) compares the displacement of the leading edge in the lubrication model to the LB simulations. The

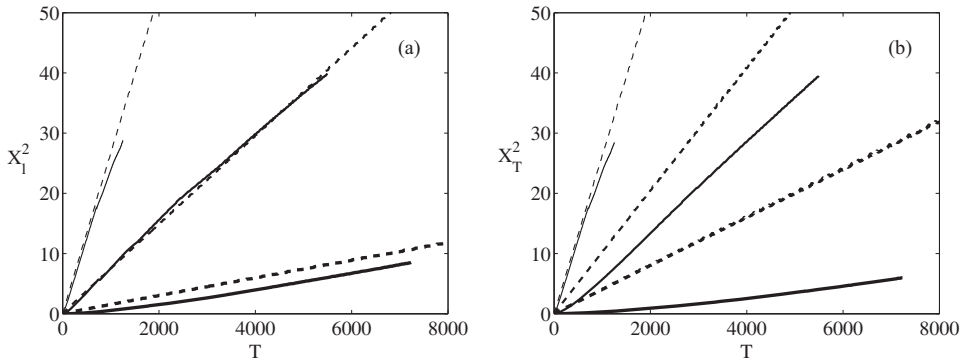

Fig. 9. Comparison of leading edge (a) and trailing edge (b) location obtained from 1D lubrication model [47] (dashed lines) and 2D simulations (solid lines). $\mu_{BT} = 1$ and $D_g = 1.74$ (——), $\mu_{BT} = 10$ and $D_g = 7.65$ (▬▬), $\mu_{BT} = 100$ and $D_g = 10.06$ (▬▬).

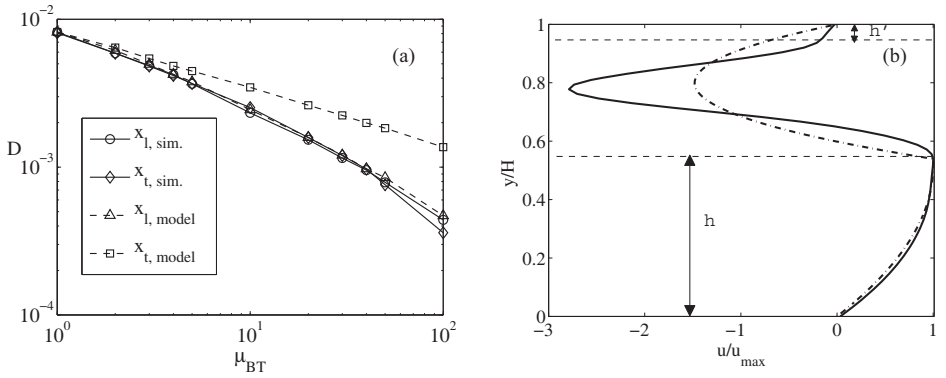

Fig. 10. Comparison of (a) diffusion coefficient for different viscosity ratios and (b) velocity profile obtained from 2D Lattice-Boltzmann simulation (——) and 1D lubrication model (— · —) where $h = 0.58$ for $\mu_{BT} = 100$.

leading edge travels at the same velocity in the lubrication model and the LB simulations for $\mu_{BT} = 1$ and 10. At long time however, the numerically obtained data deviates slightly from the curve predicted by the model owing to hydrodynamic diffusion. In the case of $\mu_{BT} = 100$, an initial transient is observed during which the gravity current does not follow a diffusive law, $X^2 \propto T$, in the simulations. The transient corresponds to an initial phase of the gravity current where the interface has a streamwise length-scale comparable to the tank height. The lubrication theory is therefore not applicable, thus explaining the mismatch at short time between the 1D lubrication model and the 2D simulations. However, the slopes of the two curves are approximately equal at long time, implying that the lubrication model predicts accurately the leading edge displacement.

The trailing edge on the other hand, shows agreement only for $\mu_{BT} = 1$ in fig. 9(b). At higher viscosity ratios $\mu_{BT} = [10, 100]$ the trailing edge travels significantly slower in the simulations than predicted by the model and the agreement worsens as the viscosity ratio is increased. This observation is further elucidated by fig. 10 which exhibits the variation in the proportionality constant, D, in

$$X^2 = DT. \tag{19}$$

The proportionality constant obtained from numerical experiments nearly coincides for the leading edge. Moreover, the proportionality constant D, corresponding to the trailing edge in simulations also concurs with the leading edge curve. The 1D model systematically overpredicts the displacement of the trailing edge as the viscosity ratio, μ_{BT}, is increased.

It is curious that the simulation data indicate that the leading edge travels according to the lubrication model prediction but not the trailing edge. In order to understand the discrepancy, the assumptions underlying eq. (17) must be reassessed. We propose a plausible explanation based on the presence of a layer of the more viscous fluid adjacent to the wall as shown in fig. 7(b). This wall layer contradicts the key assumption of the model [47] that the interface height $h(X, T)$ is a single-valued function at any given X location. As a consequence of the shape of the interface, the assumed velocity profile is also not accurate. The velocity profiles scaled by the local maximum velocity, $u_{\max}$, from the lubrication model and the LB simulation for the same value of h are compared in fig. 10(b). The figure reveals that the simulation velocity profile in the upper fluid is definitely different from that assumed by the model. Since the two velocity profiles are significantly different, the expression of the volume flux for a given pressure gradient (and thus interface gradient) evolves differently than in the case where the layer is absent. On the other hand, the wall layer is much thinner at the leading edge to have any significant effect on the spreading rate.

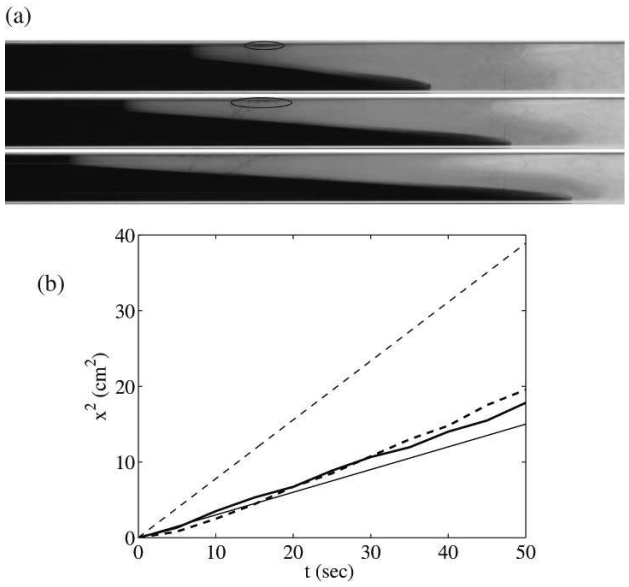

Fig. 11. (a) Snapshots of a gravity current in experiments at an interval of 5 seconds in $8 \times 8\,\mathrm{mm}^2$ cell. (b) Comparison of the leading (——) and trailing (– – –) edge displacements obtained from the lubrication model (thin lines) and experiments (thick lines) in a quasi 2D cell. $H = 3\,\mathrm{mm}$ and spanwise depth 50 mm, $\mu_{BT} \approx 100$.

The wall layer is thinner plausibly because the strain rate is very high in order to maintain shear stress continuity at the interface with the more viscous fluid, thereby preventing any significant accumulation of the less viscous fluid. Thus the displacement rate of the leading edge predicted by the model is accurate but not of the trailing edge.

3.2 Experiments

In order to ascertain the results of the LB simulations, we studied, experimentally, the lock-exchange flow between pure water and an aqueous solution of water-glycerine mixture; the viscosity ratio of the two fluids was regulated by adjusting the percentage weight of glycerine in water: the viscosity ratio is then $\mu_{BT} = 100 \pm 10$ corresponding to a density contrast $\Delta\rho = (225 \pm 5)\,\mathrm{Kg\ m^{-3}}$ at room temperature. We use two rectangular cross section cells of dimensions $8\,\mathrm{mm} \times 8\,\mathrm{mm}$ and $3\,\mathrm{mm} \times 50\,\mathrm{mm}$ respectively; the square section one is used for the sake of visualisation: Figure 11(a) shows the evolution of a viscous gravity current with a viscosity ratio, $\mu_{BT} \approx 100$. The qualitative behavior is similar to those observed in our numerical simulations, for instance the nose at the leading edge is sharp while that of the trailing edge is blunt. In addition, we observe a wall layer adjacent to the top wall (marked by the ellipse in the first snapshot of fig. 11(a)) which subsequently initiates the Rayleigh-Taylor (RT) instability. The fingers associated with the RT instability are clearly visible in the second (marked by the ellipse) and the third snapshot of fig. 11(a) behind the trailing edge. The large aspect ratio cell of height, $H = 3\,\mathrm{mm}$, has a large enough

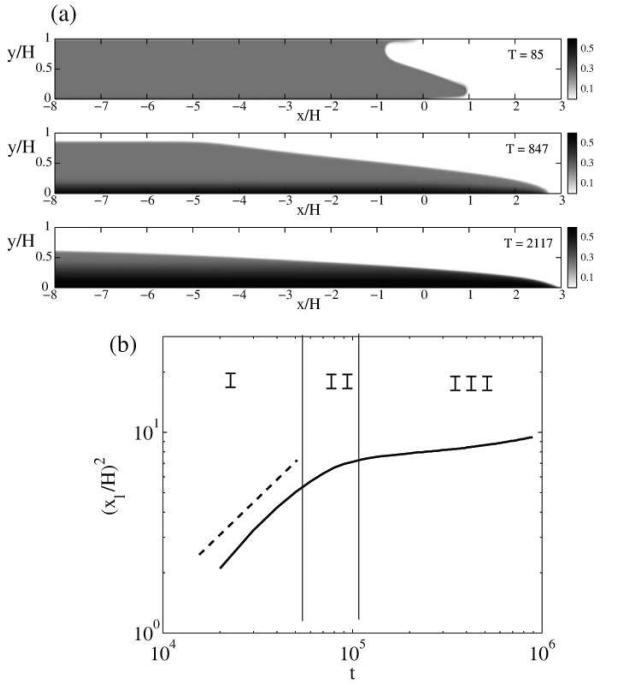

Fig. 12. Three phases in the temporal evolution of a particle-laden gravity current. (a) Concentration field in each phase. (b) Displacement of the leading edge with time. The dashed line corresponds to the slope of displacement curve of a gravity current in the absence of sedimentation. $\varphi_0 = 0.25$, $H = 128$, $u_0 = 8 \times 10^{-4}$.

spanwise depth (50 mm) to be comparable to the LB simulations [48]: a quantitative comparison of the lubrication model predictions and experimental spreading rates of the leading and trailing edges is made in fig. 11(b). Similar to the LB simulations we observe an initial transient in the data from experiments. However, at long time the displacement curves obey the law $x^2 = Dt$. The slope of the leading edge in the experiment was $(0.35 \pm 0.05)\,\mathrm{cm}^2/\mathrm{s}$ and that for the trailing edge has a slope of, $(0.4 \pm 0.05)\,\mathrm{cm}^2/\mathrm{s}$, which is nearly equal to that of the leading edge. The lubrication model predicts a leading edge diffusion coefficient $(0.3 \pm 0.05)\,\mathrm{cm}^2/\mathrm{s}$, which is in reasonable agreement with the experimental value. Hence we conclude that the observations of the LB simulation are concordant with the experiments and that the lubrication model overpredicts the spreading rate of the trailing edge.

4 Suspension gravity currents

4.1 LB Simulations

The previous section demonstrated that the viscosity of a suspension alone affects the gravity current significantly by altering the shape of the interface and modifying the characteristic velocity of spreading of the gravity current. In the presence of sedimentation, two additional fronts are created due to the settling and deposition of particles and thus the shape of the interface differs significantly from those in the previous section. Figure 12(a) presents

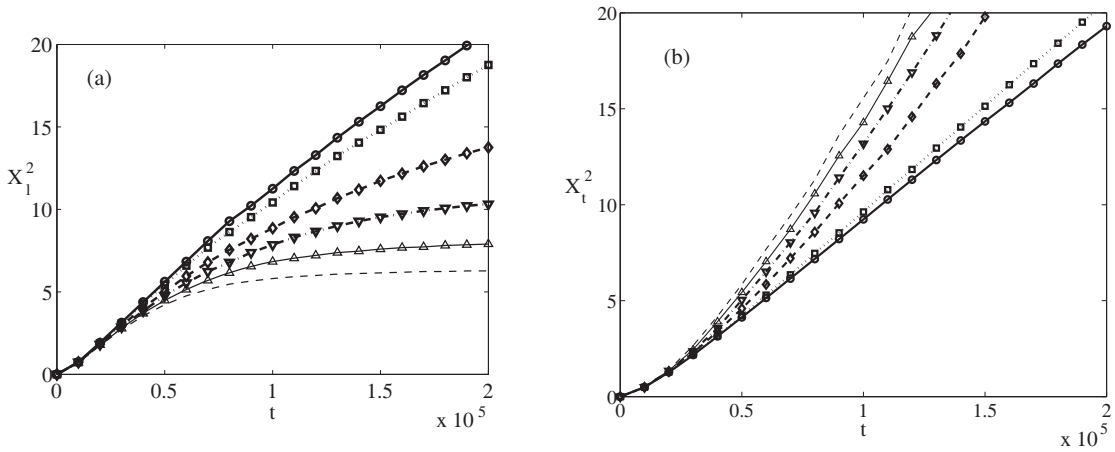

Fig. 13. (a) Reduction in the displacement of the leading edge *versus* time with increase in sedimentation velocities. (b) Increase in the displacement of the trailing edge *versus* time with increase in sedimentation velocities. $\varphi_0 = 0.3$, $H = 128$. $u_0 = 0$ (——●——); $u_0 = 1.0 \times 10^{-4}$ (· · · ·□· · · ·); $u_0 = 4.0 \times 10^{-4}$ (- - -◇- - -); $u_0 = 6.0 \times 10^{-4}$ (— · — ▽— · —); $u_0 = 8.0 \times 10^{-4}$ (——△——); $u_0 = 1.0 \times 10^{-3}$ (– – –).

the evolution of the concentration field when a suspension is released into the suspending clear fluid. There are two competing physical phenomena occurring simultaneously, a laterally spreading gravity current and a horizontal shock front due to the settling of particles which descends vertically as shown in fig. 12(a). As a result of this competition we observe three distinct phases in the spreading process. At short time, the settling front of particles is yet to be formed and the interface appears identical to a gravity current between pure fluids (Henceforth we shall refer to such currents as pure gravity currents). During the subsequent phase the particle settling front descends while the gravity current spreads, and therefore the characteristic height of the gravity current reduces thereby reducing the spreading rate compared to the previous phase. This phenomenon is elucidated by fig. 12(b) which shows the change in slope of the leading edge displacement curve compared to that of a gravity current in the absence of sedimentation. In the final stage, the leading edge nearly comes to a halt while the settling front at the top and the sediment layer continue to approach one another.

Since the extent of spreading depends on the timescale of sedimentation, we investigated the effect of Stokes velocity on the displacement characteristics. In practice, such a numerical experiment is akin to increasing the particle size in a suspension keeping the volume fraction constant. In fig. 13(a) we observe that during the first phase, the effect of sedimentation is minimal and the leading edge travels like a pure gravity current for all the cases. As the sedimentation velocity increases the displacement curve departs from the pure gravity current marginally earlier in time, indicating that the duration of the first phase also reduces slightly. Increasing the Stokes velocity curtails the displacement in the second phase and the time of transition to the third regime reduces significantly. At low u_0 the transition between the three phases is gradual and becomes increasingly sharp as the sedimentation velocity increases.

It is instructive to consider the behaviour of the trailing edge, which we define as the streamwise location where the interface height is 0.95 its maximum value. The trailing edge also departs from the pure gravity current and the instant of departure is hastened with an increase in u_0 as shown in fig. 13(b). The displacement velocity of the trailing edge increases with u_0, which is contrary to the effect of sedimentation on the leading edge. The enhancement in the front velocity of the trailing edge is due to the formation of a greater amount of clear fluid which is lighter and less viscous. As a consequence the trailing edge also travels faster with increment in the Stokes velocity.

The displacement of the leading and trailing edges depends not only on u_0 but also on the initial concentration of particles which governs the rate at which the settling front and the sediment layer approach each other. Figures 14(a) and (b) compare the spreading rates for the leading and trailing edges respectively for different values of φ_0. The results are plotted in physical coordinates since the non-dimensional coordinates (X, T) depend on φ_0 and hence mask the true behaviour of the gravity current. At this point, we recall that an increase in the particle concentration leads to reduced settling velocity of the shock front at the top. Hence the amount of clear fluid generated will also be less and therefore the rate of displacement of the trailing edge should slow down as φ_0 increases. This prediction is confirmed by fig. 14(b).

Figure 14(a) reveals that the displacement of the leading edge does not follow a monotonic trend like the trailing edge. During the first regime itself, the displacement is reduced significantly as φ_0 increases. However during the second phase we observe that the distance to which the leading edge spreads initially increases with the particle concentration and then reduces. Furthermore, the time of transition from the second to the third regime also increases initially and finally drops sharply. These observations are more evident in fig. 15(a) which shows the stoppage time, t_s, that is time of transition from phase II to phase III and the distance traversed by the leading

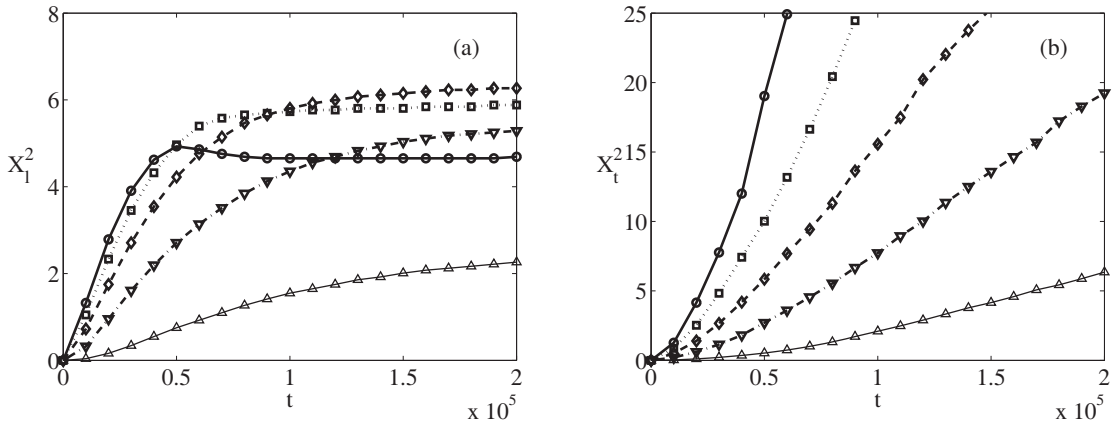

Fig. 14. (a) Leading edge and (b) trailing edge displacements at various particle concentrations. $u_0 = 0.001$, $H = 128$. $\varphi_0 = 0.1$ (—●—); $\varphi_0 = 0.2$ (···□···); $\varphi_0 = 0.3$ (- - -◇- - -); $\varphi_0 = 0.4$ (— · — ▽— · —); $\varphi_0 = 0.5$ (——△——).

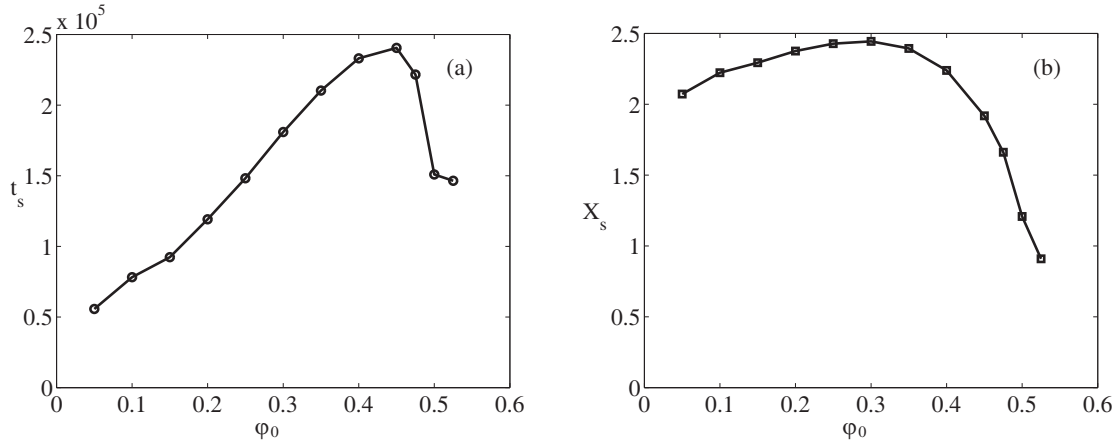

Fig. 15. (a) Stoppage time (t_s) and (b) stoppage distance x_s as a function of initial concentration φ_0, $u_0 = 0.001, H = 128$.

edge, x_s when $t = t_s$. The underlying cause of the non-monotonic behaviour of t_s and x_s is not obvious and therefore we attempt to obtain a better insight into this process by deriving a simple model based on the lubrication approximation in the following subsection.

4.2 1D lubrication model

In order to derive a model which captures the underlying physics, we assume that the flow domain can be divided into three regions of homogeneous concentration: the clear fluid, the suspension and the sediment layers. Separating these layers are two interfaces: one between the clear fluid and the suspension at a height h from the bottom and another marking the edge of the sediment layer, denoted here by h_s as shown in fig. 1. This view is supported by our numerical simulations as can be seen in fig. 12(a). Hence we can write the following concentration profile,

$$\begin{aligned} &\varphi(x,y,z,t) = 0; && y > h(x,t), \\ &\varphi(x,y,z,t) = \varphi_0; && h_s(x,t) < y < h(x,t), \\ &\varphi(x,y,z,t) = \varphi_s; && y < h_s(x,t). \end{aligned} \tag{20}$$

The assumption of a three layered profile is strictly valid for an initial condition with homogeneous concentration, φ_0. The assumption might seem to constrain the applicability of the model, but inhomogeneities in the initial concentration field are rapidly removed by "small-scale mixing motion" which occur immediately after the settling process commences [35]. Thus a uniform initial concentration field is a close approximation to a physical initial condition. It should be noted that the model derived in this section is valid only in the first and second phases. The spreading of a gravity current in the final phase will require the knowledge of the precise rheology of the suspension and is beyond the scope of this article. We intend to derive an equation governing the evolution of these fronts, for which we consider the particle transport equation (4) in the absence of hydrodynamic diffusion

$$\frac{\partial \varphi}{\partial t} + \frac{\partial}{\partial x}(u\varphi) + \frac{\partial}{\partial y}(v\varphi + \mathscr{V}\varphi) = 0. \tag{21}$$

The effect of diffusion can be ignored, as long as the time-scale of hydrodynamic diffusion, H^2/D_0, is much larger than that of sedimentation, H/u_0, thus yielding the criterion, $u_0 H/D_0 \gg 1$. Integrating eq. (21) across

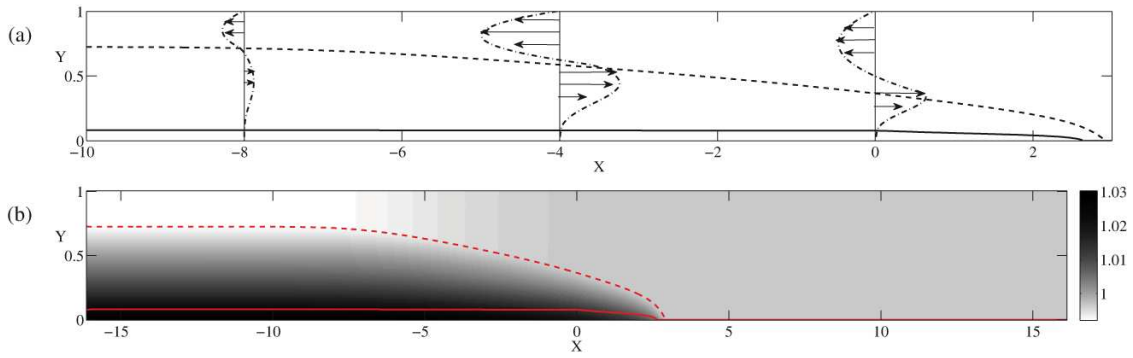

Fig. 16. (a) Velocity profiles at different locations at $t = 2 \times 10^5$. All the velocity profiles have been scaled up by a factor 10^3. $\varphi_0 = 0.25$ and $u_0 = 8 \times 10^{-4}$, $H = 128$. (b) Pressure distribution at $t = 2 \times 10^5$. The sediment layer is marked by the solid line (h_s, ——) and the top interface by the dashed line (h, – – –).

the interface, $y = h$, we have

$$\int_{h^-}^{h^+} \frac{\partial \varphi}{\partial t} \mathrm{d}y + \int_{h^-}^{h^+} \frac{\partial}{\partial x}(u\varphi)\mathrm{d}y + \int_{h^-}^{h^+} \frac{\partial}{\partial y}(v\varphi + \mathscr{V}\varphi)\mathrm{d}y = 0. \tag{22}$$

Using Leibniz's rule we arrive at

$$\frac{\partial h}{\partial t} + u(h)\frac{\partial h}{\partial x} - (v(h) + \mathcal{V}(\varphi_0)) = 0, \tag{23}$$

where $\mathcal{V}(\varphi_0)$ is given by eq. (12). Similarly we can write an evolution equation for h_s,

$$\frac{\partial h_s}{\partial t} + u(h_s)\frac{\partial h_s}{\partial x} - (v(h_s) + \mathcal{V}(\varphi_s)) = 0. \tag{24}$$

Subtracting eq. (24) from eq. (23) we have,

$$\frac{\partial}{\partial t}(h - h_s) + \underbrace{u(h)\frac{\partial h}{\partial x} - u(h_s)\frac{\partial h_s}{\partial x} - v(h) + v(h_s)}_{T_1} = \mathcal{V}(\varphi_0) - \mathcal{V}(\varphi_s). \tag{25}$$

In order to evaluate, the term T_1 we integrate the continuity equation 1 from h_s to h

$$\int_{h_s}^{h} \frac{\partial u}{\partial x}\mathrm{d}y + \int_{h_s}^{h} \frac{\partial v}{\partial y}\mathrm{d}y = 0$$
$$\Rightarrow \frac{\partial q}{\partial x} = u(h)\frac{\partial h}{\partial x} - u(h_s)\frac{\partial h_s}{\partial x} - v(h) + v(h_s), \tag{26}$$

where $q(h - h_s, \mu_{BT}) \equiv \int_{h_s}^{h} u\mathrm{d}y$. In order to derive the flux function, we assume that wall boundary conditions are applicable at $y = h_s$. Such an assumption can be justified based on the fact, that the sediment layer is extremely viscous and therefore spreads on a time-scale much larger than the suspension (or has yielded in which case it does not flow). The sediment layer is also assumed to be compacted enough to prevent any vertical penetration We can verify that applying a no-slip condition is justified at the edge of the sediment layer from fig. 16(a) which shows the velocity profiles at different locations obtained from our numerical simulations. Thus the expression for flux $q(h - h_s, \mu_{BT})$ reduces to the expression (18) in this case (see appendix A for more details). Substituting (26) into (23) leads to

$$\frac{\partial}{\partial t}(h - h_s) + \frac{\partial}{\partial x} q(h - h_s, \mu_{BT}) = \mathcal{V}(\varphi_0) - \mathcal{V}(\varphi_s). \tag{27}$$

It must be noted that, the source term in eq. (27) depends on the Stokes velocity, u_0 as can be seen from eq. (12) which in turn depends on eq. (5). Furthermore, in deriving the flux function, we assumed that the lubrication approximation is valid. The velocity profiles obtained from our numerical simulation shown in fig. 16(a) appear to be a solution to the momentum equations under the lubrication approximation. In addition, the pressure distribution shown in fig. 16(b) reveals that the local pressure field is varying linearly inside in each layer in accordance with the lubrication approximation.

Defining non-dimensional coordinates, $\tilde{h} \equiv (h - h_s)/H$, $\tau \equiv \frac{|\mathcal{V}(\varphi_0) - \mathcal{V}(\varphi_s)|t}{H}$ and $\xi \equiv \frac{x}{H}\sqrt{\frac{|\mathcal{V}(\varphi_0) - \mathcal{V}(\varphi_s)|H}{D'}}$, where $D' = \frac{(\rho_p - \rho_f)\varphi_0 g H^3}{3\mu_T}$ leads to

$$\frac{\partial \tilde{h}}{\partial \tau} + \frac{\partial}{\partial \xi}\left(f(\tilde{h}, \mu_{BT})\frac{\partial \tilde{h}}{\partial \xi} \right) = -1. \tag{28}$$

In addition we need to impose, two boundary conditions

$$\lim_{\xi \to -\infty} \frac{\partial \tilde{h}}{\partial \xi}(\xi, \tau) = 0; \tag{29}$$
$$\tilde{h}(\xi, \tau) \geq 0. \tag{30}$$

The first boundary condition (29) ensures that the sedimentation front remains flat as $\xi \to -\infty$, while the weak condition (30) implies that the height of the sediment never exceeds that of the suspension. It is instructive to consider the physical implications of the scaling ξ, which appears somewhat complicated. A closer examination reveals that the pre-factor, $\frac{|\mathcal{V}(\varphi_0) - \mathcal{V}(\varphi_s)|H}{D'}$ is the ratio of two time scales: the time-scale, H^2/D', decides the rate of lateral spreading whereas the quantity, $H/|\mathcal{V}(\varphi_0) - \mathcal{V}(\varphi_s)|$ is the time required for the two interfaces h and h_s to meet

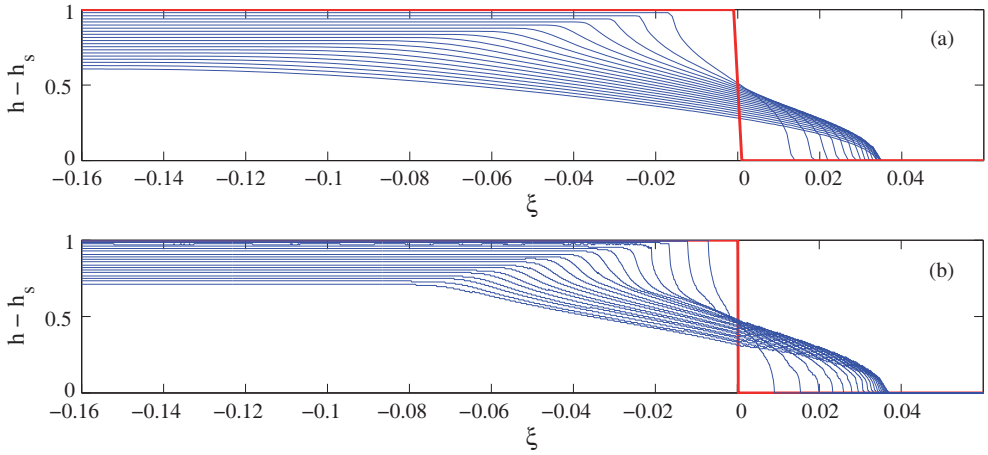

Fig. 17. Evolution of the interface with time computed from (a) 1D model (b) LB simulation for $\varphi_0 = 0.4$, $u_0 = 10^{-3}$, $H = 128$. The thick curve corresponds to the initial condition and the rest correspond to different instants of time, 0.02 time units apart.

and hence it decides when the process of sedimentation arrests. Therefore the pre-factor, indicates the displacement of the gravity current over the settling period of the suspension. It is quite noteworthy that eq. (28) has quite the same form as in the pure gravity current equation (17) except for sink term in the right hand side which takes into account the "loss" by sedimentation of particles contributing to gravity current.

The numerical solution of eq. (28), presented in fig. 17(a) reveals that the evolution of the interface between the suspension and the clear fluid is qualitatively similar to the numerical simulations in fig. 17(b) for the same parameters. The displacement of the trailing edge increases with time and that of the leading edge reduces. We also notice that the 1D lubrication model spreads faster initially than the LB simulations. This discrepancy arises because the streamwise extent of the gravity current is not much larger than the characteristic height and therefore the lubrication approximation is not valid. However, the agreement improves at the leading edge as time increases and the predicted stopping locations are in reasonably good agreement. The flat settling front on the left descends faster in the 1D model compared to the simulations. The cause of this incongruity is the reduced ascent velocity of the sediment layer, as was pointed out in fig. 3(b).

It should be noted that there exists a unique curve in our model for a given initial concentration, φ_0 and it is invariant with respect to the Stokes settling velocity u_0, which affects the shock front velocities, $|\mathcal{V}(\varphi_0) - \mathcal{V}(\varphi_s)|$ through eq. (12). In order to confirm this assertion we plot the displacement of the leading edge, ξ_l, for different u_0 in the non-dimensional coordinates ξ, τ in fig. 18(a). Indeed all the curves for leading edge displacement collapse in the first two phases of spreading for different u_0. Figure 18(b) demonstrates that the ξ_l predicted by the 1D lubrication model is in agreement with the data obtained from the 2D LB simulations for various concentrations. The displacement of the leading edge reduces significantly with increasing initial concentration due to the increment in the viscosity of the suspension.

The stoppage time, τ_s, computed from the model is compared to the data from numerical simulations over a range of initial concentrations in fig. 19(a). We observe that there is reasonable agreement between the two curves. The stoppage time is governed by the balance of two volume fluxes: First the horizontal flux driven by buoyancy which increases the height of the suspension over a certain length of the current. Second, the flux lost due to sedimentation which reduces the height of the suspension over the entire length of the current. Therefore, there is a location where the the two fluxes cancel each other out and the rate of change of the height of the suspension is instantaneously zero ($\partial\tilde{h}/\partial t = 0$). When the leading edge and the location where $\partial\tilde{h}/\partial t = 0$, coincide the current is arrested. This implies that the increase in height due to buoyancy is no longer sufficient to overcome the loss due to settling of particles. From fig. 19(a) we note that $\tau_s \approx 0.25$ and nearly constant over most of the range of concentrations investigated, indicating that

$$t_s \approx 0.25 \frac{H}{|\mathcal{V}(\varphi_0) - \mathcal{V}(\varphi_s)|}$$

$$\Rightarrow t_s \approx 0.25 \frac{\varphi_s - \varphi_0}{\varphi_s (1 - \varphi_0)^5}\,. \tag{31}$$

We re-examine fig. 15(a) in light of the expression (31). At low concentrations, t_s tends towards a constant, since the sediment layer velocity is negligible and the stopping time depends solely on the settling velocity of the shock front at the top. At concentrations $\varphi_0 \to \varphi_s$ the suspension is close to the packing fraction and therefore the sediment layer rises very quickly as shown in fig. 3(b). Thus we find that $t_s \to 0$ in this limit. In the intermediate range $\tilde{t}_s$ increases initially as the settling velocity of the shock front at the top decreases while the sediment layer velocity is nearly constant. However for $\varphi_0 > 0.45$, the function reduces drastically due to the steep rise in the velocity of the sediment layer.

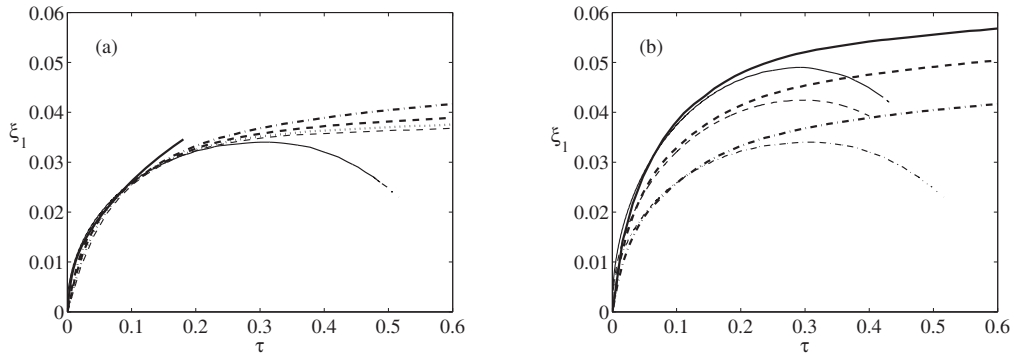

Fig. 18. (a) Comparison of the displacement of the leading edge for various Stokes velocity. 2D LB simulations: $u_0 = 2.0\times10^{-4}$ (——); $u_0 = 4.0\times10^{-4}$ (—·—); $u_0 = 6.0\times10^{-4}$ (– – –); $u_0 = 8.0\times10^{-4}$ (···); $u_0 = 1.0\times10^{-3}$ (– – –). 1D lubrication model (——) $\varphi_0 = 0.4$, $H = 128$. (b) Comparison of the displacement of the leading edge for various particle concentrations: $\varphi_0 = 0.2$ (——), $\varphi_0 = 0.3$ (···), $\varphi_0 = 0.4$ (– – –). 1D lubrication model (thin lines), 2D LB simulations (thick lines) $u_0 = 4.0\times10^{-4}$, $H = 128$.

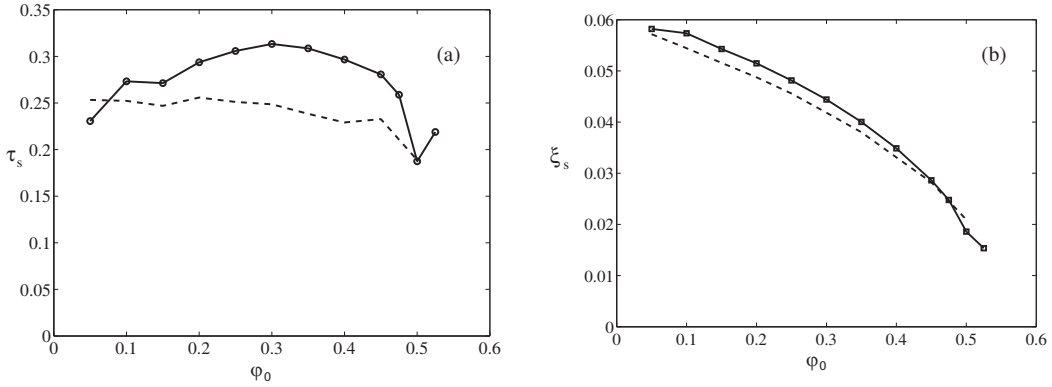

Fig. 19. Comparison of the stoppage time τ_s (a) and location ξ_s (b) from 1D lubrication model (– – –) with LB simulations (——). $u_0 = 0.001$, $H = 128$ for the LB simulations.

Figure 19(b) compares the stoppage distance ξ_s obtained from the LB simulations to the 1D lubrication model and the two match closely. In concordance with fig. 18(b) we see that ξ_s reduces as the concentration increases. The particle concentration affects the displacement in three ways: increases gravitational body force, alters the sedimentation velocity and increases the viscosity of the suspension. However, the non-dimensional plot fig. 19(b) already accounts for increasing gravity, and we also noticed that the stopping time, τ_s is nearly constant over the range of φ_0 considered. Therefore, the decrease in displacement in these coordinates can only be attributed to the increasing viscosity of the suspension. We revisit fig. 15(b) and discuss the observed behaviour of x_s in terms of the insight gained from the 1D lubrication model. In the limit $\varphi_0 \to 0$, the density difference is negligible and hence the gravity current barely spreads. Whereas when $\varphi_0 \to \varphi_s$, the suspension is nearly packed and behaves like a granular medium which resists spreading unless the driving force exceeds a certain minimum, implying that $x_s \to 0$. Furthermore, the stopping time, t_s, also reduces as we approach the limits $\varphi_0 \to 0$ or $\varphi_0 \to \varphi_s$ and thus limits the extent of spreading. Therefore a maxima can be expected in the intermediate range where the density difference is sizable, the viscosity ratio is not too large and the stopping time is close to its maximum. Indeed, such a peak exists for $\varphi_0 \approx 0.3$, as demonstrated by the LB simulations in fig. 15(b).

4.3 Experiments

In order to verify the predictions of the 1D lubrication model and the observations in our Lattice-Boltzmann simulations, we conducted experiments on particle-laden gravity currents. The experiments were performed in a rectangular cell of height $H = 20\,\text{mm}$ and depth $e = 2\,\text{mm}$; with such an aspect ratio, we are likely to be under the so-called Hele-Shaw cell regime [50], in which case it turns out that the diffusion coefficient of the gravity current can be obtained by replacing [48] H^3 by e^2H. Moreover, recent experiments [48] have demonstrated the lubrication model for the 2D problem can indeed predict the spreading rate of gravity currents in rectangular cells by multiplying the diffusion coefficient D with a prefactor $f(e/H)$. The prefactor $f(e/H)$ is determined theoretically by accounting for the boundary effects of the side walls and was substantiated by experiments [48].

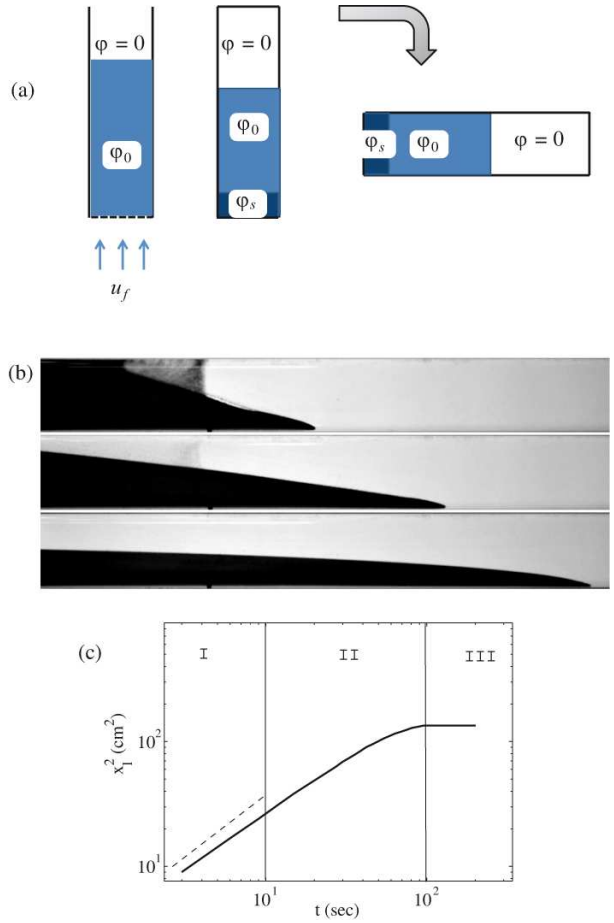

Fig. 20. (a) Schematic of the experimental setup. Snapshots (b) and the displacement of the leading edge at $t = 3\,\mathrm{s}$, $t = 27\,\mathrm{s}$ and $t = 177\,\mathrm{s}$ (from top to bottom respectively) (c) of a particle-laden gravity current in experiments showing the three phases of spreading. The gray dashed line denotes the slope corresponding to a pure gravity current. $\varphi_0 \approx 0.4$, $u_f = 0.0058\,\mathrm{mm/s}$, $u_0 = 0.11\,\mathrm{mm/s}$, $H = 20\,\mathrm{mm}$, $\rho_p - \rho_f = 1300\,\mathrm{kg/m^3}$, $\rho_f = 2500\,\mathrm{kg/m^3}$, $\mu_f = 27\,\mathrm{mPa\ s}$.

We used glass beads as suspended particles of which 95% were in the range of 63–74 μm and have a density of $2500\,\mathrm{kg/m^3}$ approximately. The fluid in which particles were suspended was an aqueous glycerine solution with 71% glycerine by weight. The suspending fluid had a density of $(1185 \pm 5)\,\mathrm{kg/m^3}$ and a viscosity (27 ± 5) m Pa s at room temperature; hence, $\rho_s - \rho_f = (1300 \pm 20)\,\mathrm{kg/m^3}$ and the Stokes velocity, $u_0 = (0.11 \pm 0.001)\,\mathrm{mm/s}$. In order to achieve a well defined concentration, we use the sedimentation cell in the configuration of a fluidized bed [38,40]: the cell is held vertically with an upwards fluid flow u_f balancing the downwards buoyancy (as sketched in fig. 20). The desired concentration, φ_0, is achieved by adjusting the flow rate (u_f) of the fluidised bed; after sufficient time, a homogeneous concentration field is achieved over the entire bed which satisfies the constraint $\mathscr{V}(\varphi_0) = (1-\varphi_0)u_f$. We then stop the flow and close both ends while keeping the cell vertical, and thereafter the suspension starts to settle with two fronts as shown in figs. 2 and 20(a). When the top front reaches the middle of the cell, we rotate the cell smoothly but rapidly by 90° to align it with the horizontal. A suspension gravity current is now set up and we record the temporal evolution.

Figure 20(b) shows the three phases of spreading of the gravity current ($\varphi_0 \approx 0.4$). During the first phase, the interface imitates a pure gravity current. However, we find that there are particles suspended in the clear fluid behind the trailing edge which is due to the side walls and the incomplete formation of the shock front between the suspension and the clear fluid. As time proceeds these suspended particles are removed by sedimentation. The second and the final phases are qualitatively similar to the numerical simulations. A quantitative measure is provided by fig. 20(c) which presents the three regimes of spreading by considering the displacement of the leading edge. A series of experiments were performed for different settling velocities of particles which correspond to different concentrations fixed by the fluid flow rate in the fluidized bed configuration. It must be noted that the suspension settling velocity decreases drastically as the concentration increases (as shown by fig. 3(a)), and therefore higher settling velocities correspond to lower concentrations. The leading edge displacement is presented in fig. 21(a). We observe that all the curves, except those for very high concentrations, are linear initially which implies that the spreading process is similar to pure gravity currents. Figure 21(b) shows that almost all the displacement curves stop at $\tau_s \in [0.2, 0.3]$ when plotted in the non-dimensional coordinates ξ, τ indicating that the 1D lubrication model is applicable to the experimental results as well.

Finally, we present the stoppage time and location of the gravity current in figs. 22(a) and (b) respectively; it is worth noting that as we use the upward flow velocity u_f of the initial vertical fluidized bed as the control parameter, the low concentration are on the right, and the ones close to the packing fraction are on the left (a plot against the tentative concentration is provided in the inset of each figure). Both figures exhibit a maximum for intermediate concentration which is in agreement with the above 1D lubrication model. Moreover, the experiments allow us to investigate the vicinity of the packing fraction; the last point on fig. 22(a) and (b) corresponds, taking into account our accuracy, to $\varphi_0 = 0.54 \pm 0.02$. An analysis of this vicinity of the packing deserves an extensive experimental study that we have postponed. The observed behaviour of t_s and x_s are similar to that in our numerical simulations.

5 Conclusion

In this article, we analysed the lock-exchange problem for a fixed volume of suspension during the viscous-buoyancy phase. In order to study the dynamics of spreading, we developed a novel numerical method to model suspensions based on laws of continuum mechanics, accounting for hydrodynamic interactions which result from increasing particle concentration. The validity of our approach was demonstrated by reproducing the enhanced sedimentation velocities observed in inclined settling chambers [44,51].

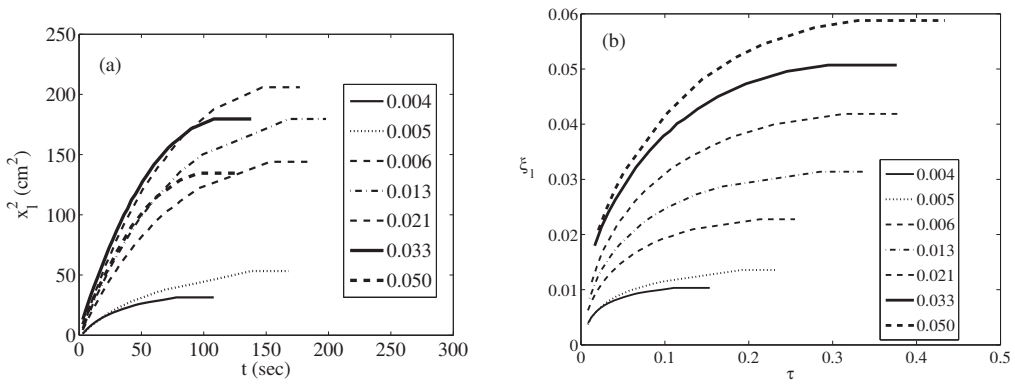

Fig. 21. (a) Experimental displacement of the leading edge for various upwards fluid velocity, u_f(mm/s), for the experimental conditions of fig. 20. (b) Displacement of the leading edge in non-dimensional coordinates.

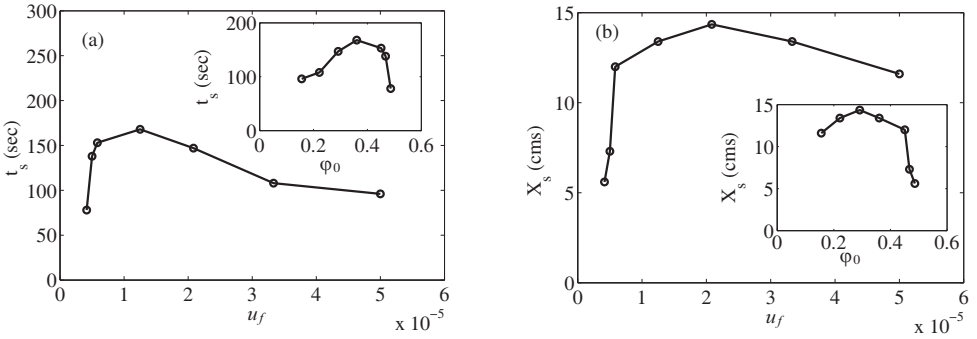

Fig. 22. (a) Stoppage time as a function of the upward flow velocity u_f of the initial vertical fluidized bed. (b) Variation in stoppage location. The inset shows the variation with φ_0 for both figures. The experimental conditions are identical to those of fig. 20.

The simplified lock-exchange between two fluids of unequal viscosities was examined numerically, to understand the effects of viscosity and gravitational body force on the spreading rates in the absence of sedimentation. It was found that the increasing the viscosity of the heavier fluid decreased the lateral spreading rate despite the increase in the body force. A comparison with the previous study [47] revealed that the current theory predicts the displacement of the leading edge fairly accurately but fails for the trailing edge. We proposed a plausible argument explaining the discrepancy, based on the presence of an additional layer of the heavy fluid adjacent to the top wall. This conclusion was further substantiated by our experiments, where such a layer was indeed found to exist.

Our numerical investigation of suspension gravity currents, demonstrated a three phase spreading process, the first being identical to lock-exchange between pure fluids. During the second phase, sedimentation controlled the spreading and the current decelerated faster than pure gravity current until it nearly came to a halt. In the final phase the sediment layer continued to flow at a relatively much slower pace than the suspension. We found that only two physical parameters, the particle size and the concentration, affect the suspension gravity current. An increase in the former keeping the concentration constant resulted in reduction of the duration of the first two phases. The effect of the latter was more complicated and a 1D lubrication model relying on the lubrication approximation was developed to gain insight. The lubrication model indicated that the extent of spreading depended on the time-scale of sedimentation and lateral diffusion coefficient (D_g) of the suspension current. This in turn implied that there exists an initial concentration $\varphi_0 \approx 0.3$ at which the stoppage distance was the maximum. This result is curiously similar to the previous experimental investigation on suspension gravity currents in the inertial-buoyancy regime [17]. We also conducted experiments in order to corroborate the findings of our numerical investigation and the results are in qualitative agreement. Future investigations will be dedicated to the studying different non-symmetric partitions [13], bidispersed suspensions [52] and evaluating the influence of the Boussinesq approximation for the inertial buoyancy currents [53,9].

The authors would like to acknowledge financial support from MULTIFLOW, Marie Curie Actions, FP7-PEOPLE PITN-GA-2008-214919 and the "Agence National de la Recherche" for fincancial support of the project LaboCothep ANR-12-MONU-0011. S.S would like to thank Prof. Howard A Stone for devoting his time to insightful discussions during his visit to Laboratory FAST.

Appendix A. The flux function under lubrication approximation

The derivation of the flux function described in this appendix is a special case of the derivation in appendix A. of [47], nevertheless we have included it for the sake of completeness. Under the lubrication approximation the velocity profile, $u(Y)$, can be assumed to be parabolic in each fluid, where $Y \equiv (y-h_s)/H$. The associated pressure field is hydrostatic in the y direction and its streamwise gradient depends on height of interface, $\tilde{h} \equiv (h-h_s)/H$. We can therefore write

$$u_T = \frac{1}{2\mu_T}\frac{\mathrm{d}P_T}{\mathrm{d}x}(Y-1)(Y-a_T), \tag{A.1}$$

$$u_B = \frac{1}{2\mu_B}\frac{\mathrm{d}P_B}{\mathrm{d}x}Y(Y-a_B), \tag{A.2}$$

where subscripts T, B refer to the clear fluid and suspension respectively. It should be noted that the velocity profiles (A.1), (A.2) already satisfy no-slip conditions at $Y=1$ and $Y=0$ respectively. The unknowns, $\frac{\mathrm{d}p_{T,B}}{\mathrm{d}x}$, $a_{T,B}$ are determined from the interfacial boundary conditions and conservation of mass. At the suspension-clear fluid interface, $Y=\tilde{h}$, continuity of velocity, tangential stress and pressure are imposed,

$$u_T - u_B = 0, \tag{A.3}$$

$$\mu_T\frac{\mathrm{d}u_T}{\mathrm{d}y} - \mu_T\frac{\mathrm{d}u_B}{\mathrm{d}y} = 0, \tag{A.4}$$

$$\frac{\mathrm{d}P_T}{\mathrm{d}x} - \frac{\mathrm{d}P_B}{\mathrm{d}x} = (\rho_p-\rho_f)\varphi_0 g\frac{\partial\tilde{h}}{\partial x} \tag{A.5}$$

and local conservation of mass requires

$$q_T + q_B = 0, \tag{A.6}$$

where $q_B \equiv \int_0^{\tilde{h}} u_B \mathrm{d}Y$ and $q_B \equiv \int_{\tilde{h}}^1 u_T \mathrm{d}Y$. Solving eqs. (A.3)-(A.6) we get

$$q_T = \frac{(\rho_p-\rho_f)\varphi_0 g H^3}{3\mu_T}\ldots \frac{\tilde{h}^3(1-\tilde{h})^3(\tilde{h}(-1+\mu_{BT})-\mu_{BT})}{(\tilde{h}^4 - 2(-1+\tilde{h})\tilde{h}(2+(-1+\tilde{h})\tilde{h})\mu_{BT} + (-1+\tilde{h})^4\mu_{BT}^2)} \times\frac{\partial\tilde{h}}{\partial x}.$$

The same derivation holds true for the flux function in eq. (18) if we put $h_s = 0$.

References

1. J. Simpson, Annu. Rev. Fluid Mech. **14**, 213 (1982).
2. H. Huppert, J. Fluid Mech. **554**, 299 (2006).
3. T. Von Karman, Bull. Am. Math. Soc **46**, 615 (1940).
4. L. Prandtl, *Essentials of Fluid Dynamics* (Hafner, New York, 1952).
5. I.R. Wood, J. Fluid Mech. **42**, 671 (1970).
6. I. Bou Malham, N. Jarrige, J. Martin, N. Rakotomalala, L. Talon, D. Salin, J. Chem. Phys. **133**, 244505 (2010).
7. N. Jarrige, I. Bou Malham, J. Martin, N. Rakotomalala, D. Salin, L. Talon, Phys. Rev. E **81**, 066311 (2010).
8. T. Séon, J. Hulin, D. Salin, B. Perrin, E. Hinch, Phys. Fluids **16**, L103 (2004).
9. T. Bonometti, S. Balachandar, J. Magnaudet, J. Fluid Mech. **616**, 445 (2008).
10. L. Talon, N. Goyal, E. Meiburg, J. Fluid Mech. **721**, 268 (2013).
11. H. Huppert, J. Shepherd, R. Haraldur Sigurdsson, S. Sparks, J. Volcanol. Geotherm. Res. **14**, 199 (1982).
12. J. Fay, Technical report, DTIC Document (1969).
13. R.T. Bonnecaze, H.E. Huppert, J.R. Lister, J. Fluid Mech. **250**, 339 (1993).
14. R. Bonnecaze, M. Hallworth, H. Huppert, J. Lister, J. Fluid Mech. **294**, 93 (1995).
15. H. Huppert, Philos. Trans.: Math. Phys. Eng. Sci. **356**, 2471 (1998).
16. E. Meiburg, B. Kneller, Annu. Rev. Fluid Mech. **42**, 135 (2010).
17. M. Hallworth, H. Huppert, Phys. Fluids **10**, 1083 (1998).
18. A. Hogg, M. Ungarish, H. Huppert, Eur. J. Mech. B-Fluids **19**, 139 (2000).
19. F. Necker, C. Härtel, L. Kleiser, E. Meiburg, J. Fluid Mech. **545**, 339 (2005).
20. M. Ungarish, *An Introduction to Gravity Currents and Intrusions* (Chapman & Hall/CRC, 2009).
21. L. Rondon, O. Pouliquen, P. Aussillous, Phys. Fluids **23**, 073301 (2011).
22. S. Mueller, E. Llewellin, H. Mader, Proc. R. Soc. A: Math. Phys. Eng. Sci. **466**, 1201 (2010).
23. G. Ovarlez, F. Bertrand, S. Rodts, J. Rheol. **50**, 259 (2006).
24. J. Brady, G. Bossis, Annu. Rev. Fluid Mech. **20**, 111 (1988).
25. P. Hoogerbrugge, J. Koelman, Europhys. Lett. **19**, 155 (1992).
26. S. Chen, G. Doolen, Annu. Rev. Fluid Mech. **30**, 329 (1998).
27. R. Glowinski, T. Pan, T. Hesla, D. Joseph, Int. J. Multiphase Flow **25**, 755 (1999).
28. J. Richardson, W. Zaki, Chem. Eng. Sci. **3**, 65 (1954).
29. G.J. Kynch, Trans. Faraday Soc. **48**, 166 (1952).
30. W. Schneider, J. Fluid Mech. **120**, 323 (1982).
31. S.H. Maron, P.E. Pierce, J. Colloid Sci. **11**, 80 (1956).
32. J. Stickel, R. Powell, Annu. Rev. Fluid Mech. **37**, 129 (2005).
33. A. Fall, F. Bertrand, G. Ovarlez, D. Bonn, Phys. Rev. Lett. **103**, 178301 (2009).
34. F. Blanc, F. Peters, E. Lemaire, J. Rheol. **55**, 835 (2011).
35. A. Acrivos, E. Herbolzheimer, J. Fluid Mech. **92**, 435 (1979).
36. E. Guazzelli, J. Hinch, Annu. Rev. Fluid Mech. **43**, 97 (2011).
37. J. Martin, N. Rakotomalala, D. Salin, Phys. Fluids **6**, 3215 (1994).
38. J. Martin, N. Rakotomalala, D. Salin, Phys. Rev. Lett. **74**, 1347 (1995).
39. J.C. Bacri, C. Frenois, M. Hoyos, R. Perzynski, N. Rakotomalala, D. Salin, Europhys. Lett. **2**, 123 (1986).

40. J. Martin, N. Rakotomalala, D. Salin, Phys. Fluids **7**, 2510 (1995).
41. I. Ginzburg, F. Verhaeghe, D. d'Humières, Commun. Comput. Phys. **3**, 427 (2008).
42. I. Ginzburg, D. d'Humières, A. Kuzmin, J. Stat. Phys. **139**, 1090 (2010).
43. G. Whitham, *Linear and Nonlinear Waves* (John Wiley & Sons, 1999).
44. A.E. Boycott, Nature **104**, 532 (1920).
45. E. Ponder, Q. J. Expt. Physiol. **15**, 235 (1925).
46. H. Nakamura, K. Kuroda, Keijo J. Med. **8**, 235 (1937).
47. S.M. Taghavi, T. Seon, D.M. Martinez, I.A. Frigaard, J. Fluid Mech. **639**, 1 (2009).
48. J. Martin, N. Rakotomalala, L. Talon, D. Salin, J. Fluid Mech. **673**, 132 (2011).
49. H. Huppert, J. Fluid Mech. **121**, 43 (1982).
50. J. Zeng, Y.C. Yortsos, D. Salin, Phys. Fluids **15**, 3829 (2003).
51. A. Acrivos, E. Herbolzheimer, J. Fluid Mech. **92**, 435 (1979).
52. M. Hoyos, J.C. Bacri, J. Martin, D. Salin, Phys. Fluids **6**, 3809 (1994).
53. V.K. Birman, J.E. Martin, E. Meiburg, J. Fluid Mech. **537**, 125 (2005).